AIMS Materials Science, 12(5): 1004–1024.
DOI: 10.3934/matersci.2025046
Received: 29 July 2025
Revised: 18 September 2025
Accepted: 22 September 2025
Published: 13 October 2025

https://www.aimspress.com/journal/Materials

Research article

Optimization of HTL and ETL materials and parameters for high-efficiency $CH_3NH_3SnI_3$ perovskite solar cells

Ala'eddin A. Saif* and Ghalyiah Alahmadi

Department of Physical Sciences, College of Science, University of Jeddah, Jeddah, Saudi Arabia

* **Correspondence:** Email: aasaif@uj.edu.sa; Tel: +966-59-5120-706.

Abstract: This study explored how varying the material and physical properties of the electron transport layer (ETL) and hole transport layer (HTL) layers affects the performance of $CH_3NH_3SnI_3$ perovskite solar cells. Numerical simulations were conducted using 1D Solar Cell Capacity Simulator (SCAPS-1D) software, with the AM1.5G solar spectrum at an intensity of 1000 W/m^2 applied from the ETL side. The simulation started with the structure fluorine-doped tin oxide (FTO)/ETL/$CH_3NH_3SnI_3$/HTL/Ni, where ZnO_2 was assigned as the ETL layer and CuSCN as the HTL layer. Then, different materials were suggested to act as the ETL and HTL layers. Finally, the doping and thickness of the best material obtained for the ETL and HTL layers were optimized. The results reveal that WS_2 is the most promising for the ETL, while $CuSbS_2$ was identified as the most suitable material for the HTL in $CH_3NH_3SnI_3$ solar cells. By increasing the doping levels and layer thicknesses of the ETL and HTL, the conversion efficiency of the solar cell was slightly enhanced. The electrical performance of the $CH_3NH_3SnI_3$ solar cell showed significant improvement compared to the initial configuration: the V_{oc} increased from 1.024 to 1.042 V, J_{sc} slightly increased from 33.86 to 33.92 mA/cm^2, the fill factor improved from 76.17% to 84.29%, and the overall efficiency (η) increased from 26.42% to 29.8%. This study highlights how material and structural optimizations can improve the performance of $CH_3NH_3SnI_3$ perovskite solar cells, offering valuable insights for the future design of high-efficiency perovskite photovoltaics.

Keywords: perovskite solar cells; SCAPS-1D; $CH_3NH_3SnI_3$; ETL; HTL

1. Introduction

Energy obtained from renewable sources is acknowledged as an environmentally friendly and sustainable alternative to fossil fuels, resulting in substantial advancements in its collection and usage [1]. Perovskite solar cells (PSCs) have been recognized as a highly promising photovoltaic technology, in comparison with other kinds of solar cells, due to their exceptional power conversion efficiency, solution processability, and comparatively low fabrication costs [2]. For a decade of research, perovskite solar cells demonstrated remarkable promise, achieving power conversion efficiencies exceeding 25% [3]. Despite this improvement, most high-performing PSCs still use lead-based perovskites as absorbers, which raises concerns about potential adverse impacts on the environment and sustainability consequences.

The low toxicity, high absorption coefficient, and outstanding optoelectronic properties of tin-based perovskite have made it a highly promising alternative to lead perovskite, garnering significant attention [4]. Methylammonium tin iodide ($CH_3NH_3SnI_3$) is recommended as a lead-free alternative that is suitable for optimal solar energy absorption due to its reasonable energy bandgap (1.3–1.4 eV) [5]. Despite $CH_3NH_3SnI_3$ being environmentally friendly, the effectiveness of $CH_3NH_3SnI_3$ is limited due to its instability, large defect concentrations, and inadequate carrier lifetimes [6]. These challenges necessitate systematic optimization strategies for maximizing its potential.

An essential factor in enhancing the performance and stability of Sn-based PSCs is the optimization of the charge transport layers. The electron transport layer (ETL) and the hole transport layer (HTL) are crucial in controlling carrier extraction, reducing recombination losses, and optimizing the delivery of charge carriers to the contacts [2]. Recent evaluations have underscored advancements in ETL and HTL engineering for tin-lead PSCs, illustrating how optimal material selection and parameter optimization directly influence efficiency and device durability [7]. Besides, enhancements in energy level alignment, defect passivation, and carrier mobility in the transport layer have been documented to substantially elevate overall device performance [8]. Interfacial passivation has been studied in recent research to greatly enhance carrier transport and stability. A self-formed $SnCl_2$ passivation layer on SnO_2 ETL effectively minimizes defects and enhances device stability, as reported by Howlader et al. [9]. Additionally, a study on double-sided passivated PSCs showed a significant reduction in photovoltaic loss and increased durability [10]. These results underscore the significance of transport layer selection and interfacial engineering for optimal performance of perovskite devices.

This study aims to optimize the parameters of the ETL and HTL layers in $CH_3NH_3SnI_3$-based perovskite solar cells by numerical modeling. The investigation begins with identifying a suitable material configuration for use as ETL and HTL, followed by a systematic examination of how carrier injection level and layer thickness of both the ETL and HTL impact the device performance.

2. Materials and methods

The 1D Solar Cell Capacity Simulator (SCAPS-1D) software is the most frequently used solar cell simulator [11,12]. It provides simulation-based solutions for fundamental semiconductor equations, including the continuity equation, Poisson's equation, and the carrier transport equations governing charge dynamics [13]. Many scholars have validated it by comparing the findings acquired from simulation with the results gained from experiments [14,15].

As can be seen in Figure 1, the simulation in this work begins with the structure fluorine-doped tin oxide (FTO)/ETL/$CH_3NH_3SnI_3$/HTL/Ni. The front electrode is made of a transparent FTO material with 0.5 µm thickness, and the rear metal electrode is made of Ni. In the initial solar cell, the ETL is allocated to ZnO_2 with a thickness of 0.03 µm, while the HTL is assigned to CuSCN with a thickness of 0.05 µm. Table 1 provides a quick summary of the material parameters for each layer. Table 2 contains a tabulation of the defect interface characteristics at the ZnO_2/$CH_3NH_3SnI_3$ and $CH_3NH_3SnI_3$/CuSCN interfaces. At a temperature of 300 K, the modeling procedure is carried out using the radiation of the AM1.5G solar radiation spectrum, with a power density of 1000 W/m^2 coming from the ETL side. The absorption coefficient of the $CH_3NH_3SnI_3$ active layer is modeled using the built-in $(hv-E_g)^{1/2}$ law option in SCAPS-1D, where the bandgap E_g is set to 1.3 eV.

The influence of variation of the ETL and HTL layer compositions on the proposed basic solar cell performance is investigated. The suggested materials for the ETL layer are WS_2, ZnO_2, IGZO, ZnMgO, CdS, ZnSe, and In_2S_3, while the materials for the HTL layer include $CuSbS_2$, Cu_2O, CuSCN, MoS_2, CuI, ZnTe, and Spiro. The impact of variation of the thickness and doping of the optimum materials of the HTL and ETL is also studied. The doping concentrations of ETL and HTL are systematically varied across a wide range (10^{14}–10^{21} cm^{-3}) to investigate their effects on carrier transport and recombination. Whereas these values are numerically established in SCAPS-1D, they represent conditions that can be experimentally achieved. Doping in transport layers is typically achieved via precursor engineering, chemical additives, or inserting additional doped interfacial or nanoparticle layers [16,17].

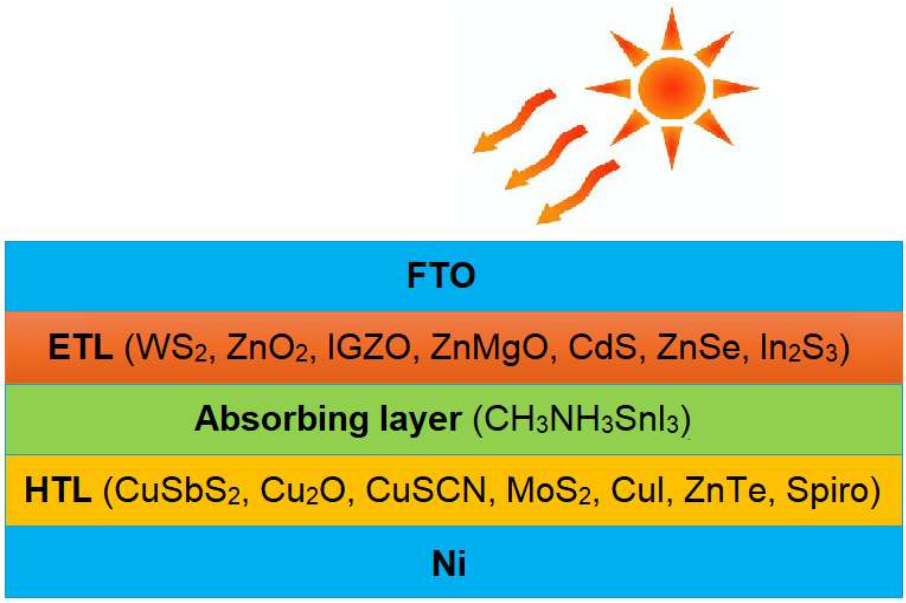

Figure 1. Initial solar cell structure.

Table 1. Input parameters of the initial solar cell.

Parameters	FTO [18]	ZnO_2 [19]	$CH_3NH_3SnI_3$ [18]	CuSCN [19]
E_g (eV)	3.5	3.3	1.3	3.4
χ (eV)	4	4.1	4.2	1.9
ε_r	9	9	10	10
N_c (cm^{-3})	2×10^{18}	4×10^{18}	1×10^{18}	1.7×10^{19}
N_v (cm^{-3})	1.8×10^{19}	1×10^{19}	1×10^{18}	2.5×10^{21}
μ_n (cm^2/vs)	20	100	1.6	1×10^{-4}
μ_p (cm^2/vs)	10	25	1.6	1×10^{-1}
N_D (cm^{-3})	2×10^{19}	1×10^{18}	0	0
N_A (cm^{-3})	0	0	3.2×10^{15}	1×10^{18}
N_t	1×10^{15}	1×10^{15}	1×10^{14}	1×10^{14}

Table 2. Layer interface parameters.

Parameters	$CH_3NH_3SnI_3$/CuSCN	$ZnO_2/CH_3NH_3SnI_3$
Defect type	Neutral	Neutral
Capture cross-section electrons/holes (cm^2)	1×10^{19}	1×10^{19}
	1×10^{19}	1×10^{19}
Energetic distribution	Single	Single
Reference of defect energy level (E_t)	Above the EV maximum	Above the EV maximum
Total density (cm^{-2})	1×10^{10}	1×10^{10}

3. Results and discussion

3.1. Basic solar cell

The J-V curve of the initial $CH_3NH_3SnI_3$ solar cell using the parameters from Tables 1 and 2 via SCAPS software is shown in Figure 2a. Data indicate that the conversion efficiency of the basic cell is 26.42%. Figure 2b illustrates the dependence of the external quantum efficiency (EQE) of the initial solar cell on wavelength. As the wavelength increases from 300 to 360 nm, the EQE of the initial cell shows a substantial increase from 44% to 98.99%. Afterward, the EQE maintains a relatively stable value until reaching 600 nm, after which it gradually declines to 81.87% at a wavelength of 900 nm. The EQE encompasses the complete range of the visible spectrum due to the $CH_3NH_3SnI_3$ tiny energy bandgap.

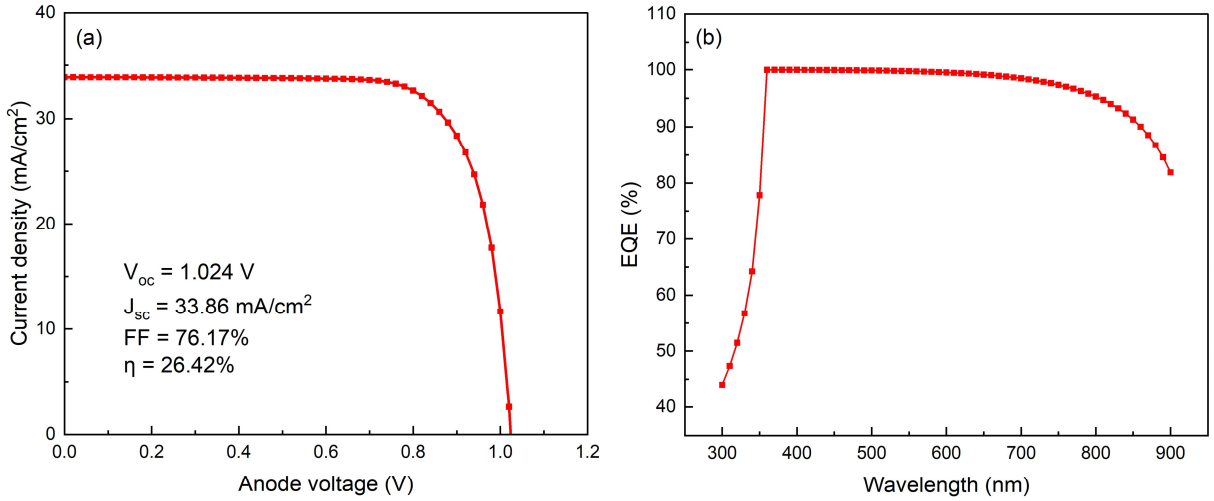

Figure 2. (a) J-V characteristics and (b) efficiency versus wavelength of the initial cell.

3.2. Impact of ETL material

To minimize energy loss, the ETL layer should have a larger energy bandgap than the perovskite layer, ensuring that lower energy photons reach the absorber layer. In addition, the ETL layer enables transporting the photogenerated electrons from the perovskite layer while preventing the movement of holes to minimize the rate of charge recombination [20]. Thus, it is crucial for the energy levels of the material to be compatible with those of the perovskite absorber layer to ensure efficient electron flow to the front contact. The study examines various ETL materials, including WS_2, ZnMgO, ZnSe, CdS, IGZO, and In_2S_3, in conjunction with CuSCN as the HTL layer. The physical variables of the substances utilized are summarized in Table 3.

Table 3. Input parameters of the ETL materials.

Parameters	ZnSe [5]	IGZO [5]	In_2S_3 [22]	CdS [22]	ZnO_2 [22]	ZnMgO [23]	WS_2 [23]
E_g (eV)	2.81	3.05	2.45	2.4	3.3	3.33	1.8
χ (eV)	4.09	4.16	3.98	4.18	4.1	3.9	3.95
ε_r	8.6	10	6.5	10	9	9	13.6
N_c (cm^{-3})	2.2×10^{18}	5×10^{18}	1.8×10^{19}	2.2×10^{18}	5×10^{18}	1×10^{21}	2×10^{18}
N_v (cm^{-3})	1.8×10^{19}	5×10^{18}	4×10^{13}	1.9×10^{19}	1×10^{19}	2×10^{20}	1×10^{19}
μ_n (cm^2/vs)	400	15	400	100	100	20	100
μ_p (cm^2/vs)	110	0.1	210	25	25	10	100
N_D (cm^{-3})	1×10^{18}	1×10^{18}	1×10^{18}	1×10^{18}	1×10^{18}	1×10^{18}	1×10^{18}
N_A (cm^{-3})	0	0	0	0	0	0	0
N_t	1×10^{15}	1×10^{15}	1×10^{15}	1×10^{15}	1×10^{15}	1×10^{15}	1×10^{15}

Figure 3a displays the J-V curves of all cells constructed using the proposed materials as the ETL. All suggested materials exhibit nearly similar J-V characteristics. This is further supported by the electrical characteristics of these solar cells, which are provided in Table 4. The functionality of the

$CH_3NH_3SnI_3$ solar cell is minimally influenced by the proposed ETL materials when CuSCN serves as the HTL layer. Nevertheless, WS_2 exhibits marginally greater short circuit current and conversion efficiency than the other materials. This is correlated to the high conductivity and transparency of WS_2 [21]. Figure 3b displays the variation of the EQE versus the wavelength of $CH_3NH_3SnI_3$ solar cells with various ETL materials. All materials, except for In_2S_3, exhibit similar behavior to the initial solar cell. However, In_2S_3 displays lower EQE values within the range of wavelengths between 300 and 360 nm. The decline in EQE at wavelengths below ~380 nm is due to absorption in the FTO and ETL layers, where high-energy UV photons are absorbed prior to reaching the $CH_3NH_3SnI_3$ absorber, thereby diminishing the carrier production from this spectral area.

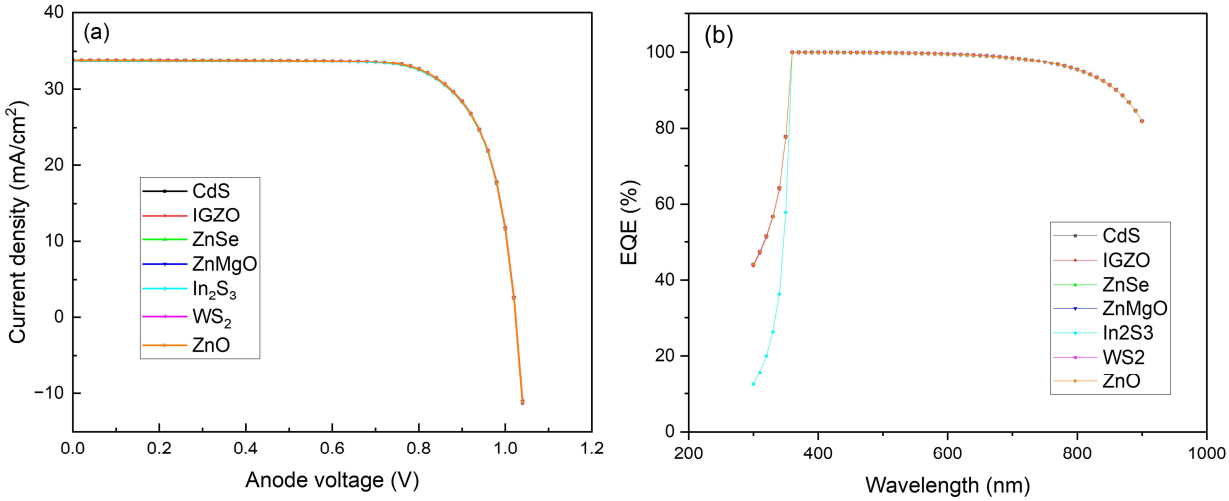

Figure 3. (a) J-V characteristics and (b) quantum efficiency versus wavelength of solar cells at different ETL materials using CuSCN as the HTL.

Table 4. Solar cells' parameters with various ETL materials.

Device structure	J_{sc} (mA/cm^2)	V_{oc} (V)	FF (%)	η (%)
FTO/ZnO/$CH_3NH_3SnI_3$/CuSCN/Ni	33.861	1.024	76.17	26.42
FTO/CdS/$CH_3NH_3SnI_3$/CuSCN/Ni	33.861	1.024	76.16	26.41
FTO/In_2S_3/$CH_3NH_3SnI_3$/CuSCN/Ni	33.753	1.024	76.18	26.43
FTO/WS_2/$CH_3NH_3SnI_3$/CuSCN/Ni	33.867	1.024	76.18	26.43
FTO/ZnSe/$CH_3NH_3SnI_3$/CuSCN/Ni	33.861	1.024	76.18	26.42
FTO/IGZO/$CH_3NH_3SnI_3$/CuSCN/Ni	33.859	1.024	76.16	26.41
FTO/ZnMgO/$CH_3NH_3SnI_3$/CuSCN/Ni	33.861	1.024	76.17	26.42

For further discussion of the influence of different ETL materials, the photogeneration rate as a function of the solar cells' depth is plotted in Figure 4a. It can be seen that the incident light is transmitted through the FTO electrode into the ETL layer and then is partially absorbed within the ETL layer as carriers start to generate in this region. Comparably, WS_2 can generate carriers at a higher rate than the other materials due to its low energy bandgap. In addition, due to the absorption of some wavelengths corresponding to the bandgap in the ETL region, a lower photogeneration rate with the perovskite $CH_3NH_3SnI_3$ layer is obtained.

The recombination rate as a function of the solar cells' depth of different ETL materials is plotted in Figure 4b. It is visible that the recombination rate within the ETL and $CH_3NH_3SnI_3$ active layer varies with the ETL material; the lowest recombination rate in $CH_3NH_3SnI_3$ is obtained when WS_2 is utilized as ETL. This confirms the selection of WS_2 as the most promising ETL material among the other suggested materials.

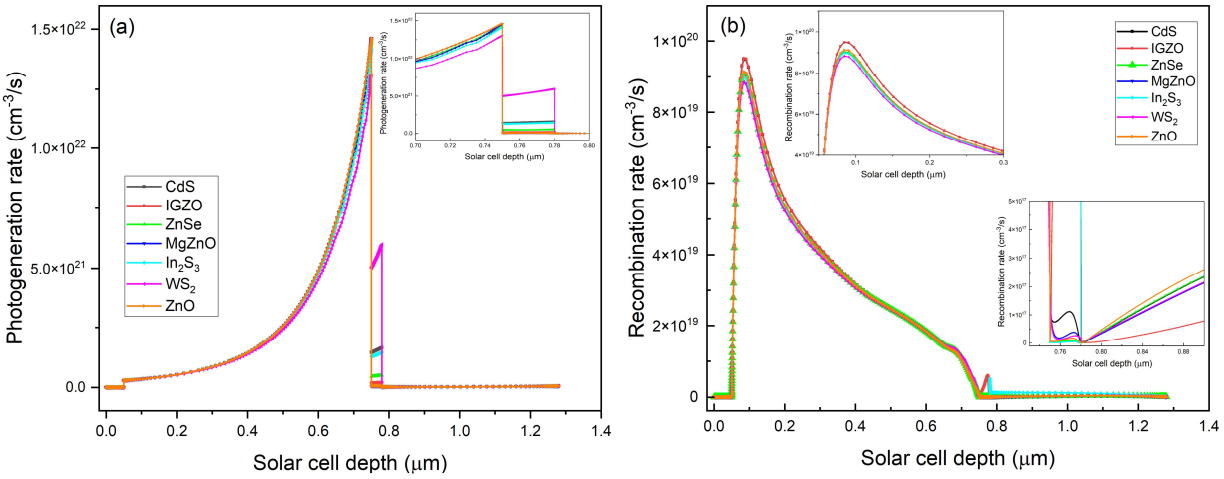

Figure 4. (a) Photogeneration and (b) recombination rate of $CH_3NH_3SnI_3$ solar cell at different ETL materials.

For further understanding of the impact of the ETL material on the $CH_3NH_3SnI_3$ solar cell, the energy band diagrams corresponding to different ETL materials are plotted, as shown in Figure 5. It is clear that the energy band diagram of all cells is identical except within the ETL layer, where it shows some variation in the conduction and valence bands, which are expanded in the inset figures. To interpret the variation in efficiency with ETL material, the conduction band and valence band energy offsets between the perovskite and the adjacent layers are calculated and tabulated in Table 5. It is believed that the higher energy difference between the conduction bands of $CH_3NH_3SnI_3$ and ETL layers indicates easier movement of the photogenerated electrons from the perovskite material to the front electrode. Besides, the higher energy difference between the valence bands of the electrode and the ETL layers leads to fewer holes being able to reach the perovskite layer and recombine with the electrons generated there. Based on this theory, WS_2 represents the most suitable material to be utilized as the ETL to guarantee less recombination within the absorbing material.

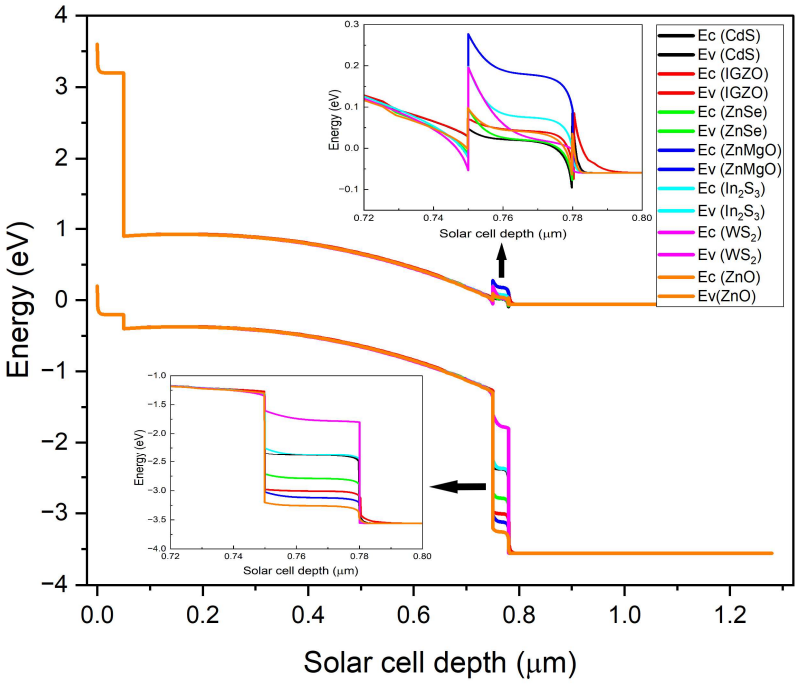

Figure 5. Energy band structure of $CH_3NH_3SnI_3$ solar cells with various ETL materials.

Table 5. Energy band differences between $CH_3NH_3SnI_3$ and the ETL and between the ETL and FTO layers.

ETL material	Conduction band offset between $CH_3NH_3SnI_3$ and ETL (eV)	Valence band offset between ETL and FTO (eV)
WS_2	0.0972	1.781
ZnO	0.0733	1.183
CdS	0.1106	1.183
In_2S_3	0.0497	0.767
IGZO	0.0818	0.55
ZnSe	0.0492	0.436
ZnMgO	–0.0533	0.297

3.3. Impact of the HTL material

The primary function of the HTL in perovskite solar cells is to ease the movement of holes out of the active perovskite layer to the rear contact while also serving as a barrier to impede the passage of the electrons [24]. The HTL layer also serves to shield the perovskite active layer from air moisture, hence improving the long-term durability of the solar cell [25]. Thus, choosing an HTL material that has favorable compatibility of the valence bands with the perovskite enhances the extraction and delivery of holes, thereby increasing the short-circuit current density and ultimately enhancing the overall cell efficiency [26]. This work examines the influence of different HTL materials on the performance of the $CH_3NH_3SnI_3$ solar cell, upon choosing WS_2 as the most suitable ETL substance. A variety of materials, such as $CuSbS_2$, Cu_2O, CuSCN, MoS_2, CuI, ZnTe, and Spiro-OMeTAD, have

been examined in the presence of WS_2 as the ETL. The physical parameters of these materials utilized for simulation are succinctly presented in Table 6.

Table 6. Input parameters of HTL materials.

Parameters	ZnTe [23]	$CuSbS_2$ [27]	Spiro [22]	CuI [19]	Cu_2O [19]	MoS_2 [18]
E_g (eV)	2.25	1.58	3	3.1	2.17	1.29
χ (eV)	3.73	4.2	2.45	2.1	3.2	4.2
ε_r	7.3	14.6	3	6.5	7.1	3
N_c (cm^{-3})	1.17×10^{18}	2.0×10^{18}	1×10^{19}	2.8×10^{19}	2×10^{17}	2.2×10^{18}
N_v (cm^{-3})	1.66×10^{19}	1.0×10^{19}	1×10^{19}	1×10^{19}	1.1×10^{19}	1.8×10^{19}
μ_n (cm^2/vs)	300	49	2×10^{-4}	100	200	100
μ_p (cm^2/vs)	100	49	2×10^{-4}	43.9	80	150
N_D (cm^{-3})	0	0	0	0	0	0
N_A (cm^{-3})	1×10^{18}	1.38×10^{18}	1×10^{18}	1×10^{18}	1×10^{18}	1×10^{18}
N_t	1×10^{14}	1×10^{14}	1×10^{14}	1×10^{14}	1×10^{14}	1×10^{14}

Figure 6a displays the J-V characteristics of the $CH_3NH_3SnI_3$ perovskite solar cell utilizing various HTL materials, while WS_2 serves as the ETL. The short circuit current for all solar cells using various HTL materials is nearly identical. Nevertheless, fluctuations exist in both the open circuit voltage and the maximum power point (MPP). The CuI and CuSCN cells exhibit a comparable low fill factor and efficiency values, as shown in Table 7, because of their low maximum power point. The low value of η of the solar cell, when MoS_2 is utilized as the HTL, is attributed to its low V_{oc} value of 0.965, which is lower than that of the other cells. Table 7 shows that the solar cell with $CuSbS_2$ has the best conversion efficiency among the HTL materials used. Figure 6b shows the relation between the wavelength of solar cells and the EQE for various HTL materials, with WS_2 serving as the ETL. It is evident that all cells exhibit the same external quantum efficiency pattern and values as the original solar cell, except for the cell with ZnTe HTL, which demonstrates poorer efficiency within the visible spectrum compared to the other cells.

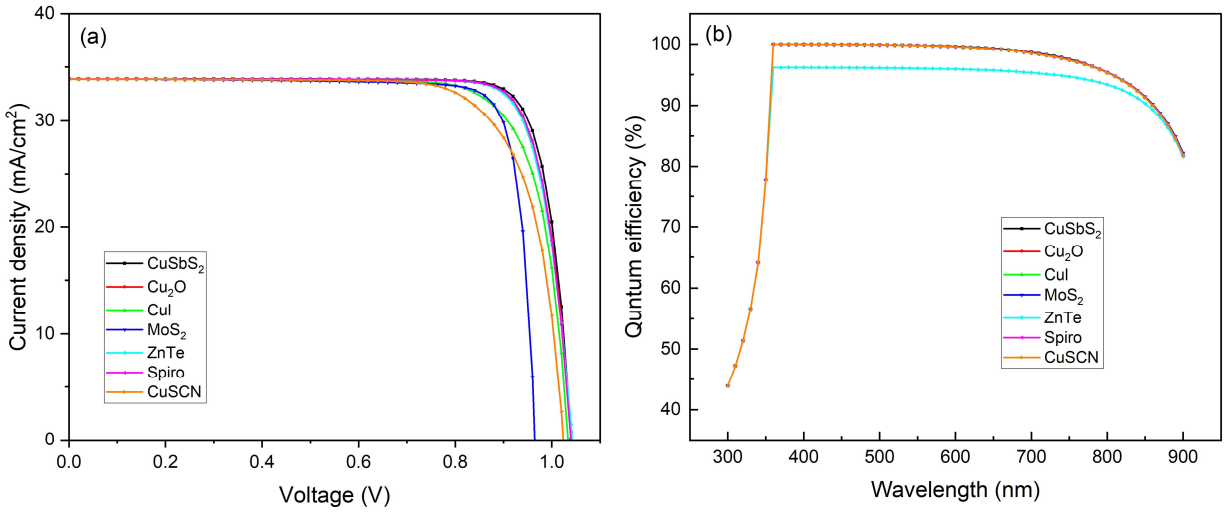

Figure 6. (a) J-V characteristics and (b) quantum efficiency versus wavelength of solar cells at different HTL materials using WS_2 as the HTL.

Table 7. Cell parameters at different HTL materials using WS_2 as the ETL.

Solar cell	J_{sc} (mA/cm^2)	V_{oc} (V)	FF (%)	Eff (%)
FTO/WS_2/$CH_3NH_3SnI_3$/$CuSbS_2$/Ni	33.889	1.040	84.33	29.75
FTO/WS_2/$CH_3NH_3SnI_3$/Cu_2O/Ni	33.874	1.040	83.32	29.36
FTO/WS_2/$CH_3NH_3SnI_3$/Spiro/Ni	33.874	1.039	83.70	29.48
FTO/WS_2/$CH_3NH_3SnI_3$/CuI/Ni	33.868	1.034	78.97	27.66
FTO/WS_2/$CH_3NH_3SnI_3$/MoS_2/Ni	33.889	0.965	88.22	27.88
FTO/WS_2/$CH_3NH_3SnI_3$/ZnTe/Ni	33.875	1.042	83.00	29.31
FTO/WS_2/$CH_3NH_3SnI_3$/CuSCN/Ni	33.867	1.024	76.18	26.43

To investigate the impact of various HTL materials on the functioning of the $CH_3NH_3SnI_3$ solar cell, the profile of the photogeneration rate of the cells with various HTL materials is plotted versus the solar cell depth, as shown in Figure 7a. It is obvious that the photogeneration along all solar cells is identical except for the MoS_2, since its energy bandgap is slightly higher than that of the other HTL materials. This allows it to absorb long wavelengths; thus, further carriers will be generated within the MoS_2 HTL layer. The recombination rate of the $CH_3NH_3SnI_3$ solar cells utilizing different HTL materials along the cells' depth is plotted in Figure 7b, which illustrates that the solar cell using $CuSbS_2$ HTL has the minimum recombination rate within the absorber layer compared to the other HTL materials. This indicates that the $CH_3NH_3SnI_3$ solar cell using $CuSbS_2$ as the HTL would have the best performance, which is in line with the results obtained in Table 7.

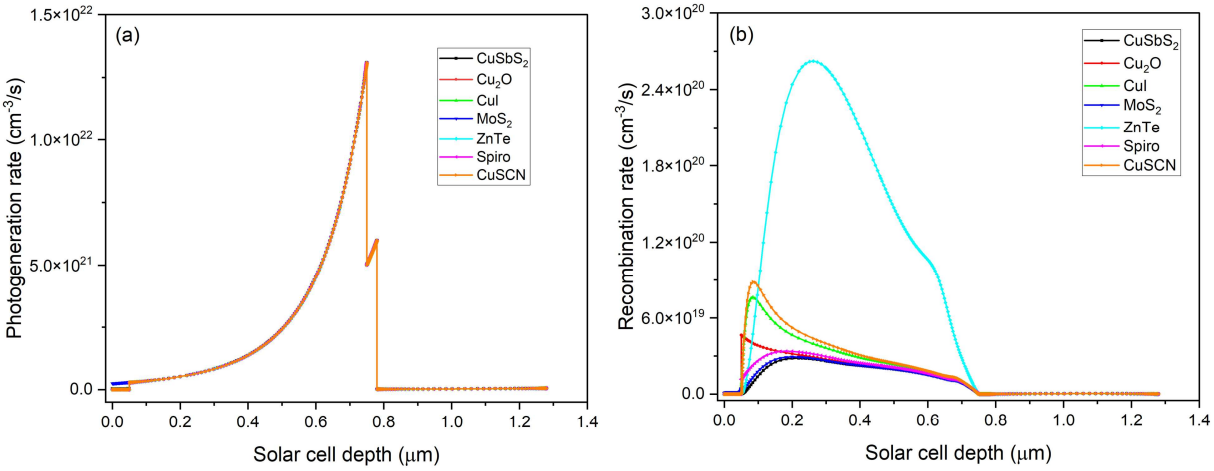

Figure 7. (a) Photogeneration and (b) recombination rate of $CH_3NH_3SnI_3$ solar cell at different HTL materials.

For further investigation of selecting $CuSbS_2$ as the best HTL material, the energy band structure along the $CH_3NH_3SnI_3$ solar cells with various HTL candidates is plotted in Figure 8. The main role of the HTL layer is to facilitate the transport of photogenerated holes from the absorber layer to the back electrode, in addition to preventing the electrons from passing from the back electrode toward the perovskite layer, to avoid carriers' recombination as much as possible. To evaluate this, two key parameters are analyzed: (i) the valence band energy offset between the HTL and $CH_3NH_3SnI_3$ absorber, and (ii) the Ni/HTL contact barrier. The results are summarized in Table 8. From the table, it is seen that $CuSbS_2$ provides the most favorable alignment. It possesses the smallest valence band offset with $CH_3NH_3SnI_3$ (0.056 eV), which facilitates hole transfer at the absorber/HTL interface, and a negative hole barrier with Ni electrode (–0.28 eV), indicating an ohmic contact with the back electrode. This dual advantage explains the comparable low recombination rate for $CuSbS_2$ observed in Figure 7b. By contrast, CuI exhibits a relatively small valence offset but suffers from a large barrier height (0.36 eV), which creates a barrier for hole transfer and increases recombination. ZnTe presents the opposite problem: although it forms an ohmic contact with Ni/HTL (barrier height = –0.48 eV), its large valence offset (0.791 eV) severely resists hole transfer at the absorber/HTL interface, leading to high recombination. Overall, $CuSbS_2$ is considered the most appropriate material to be used, combining excellent band alignment with $CH_3NH_3SnI_3$ and a favorable ohmic Ni contact, guaranteeing efficient hole extraction and minimal recombination compared to the other materials.

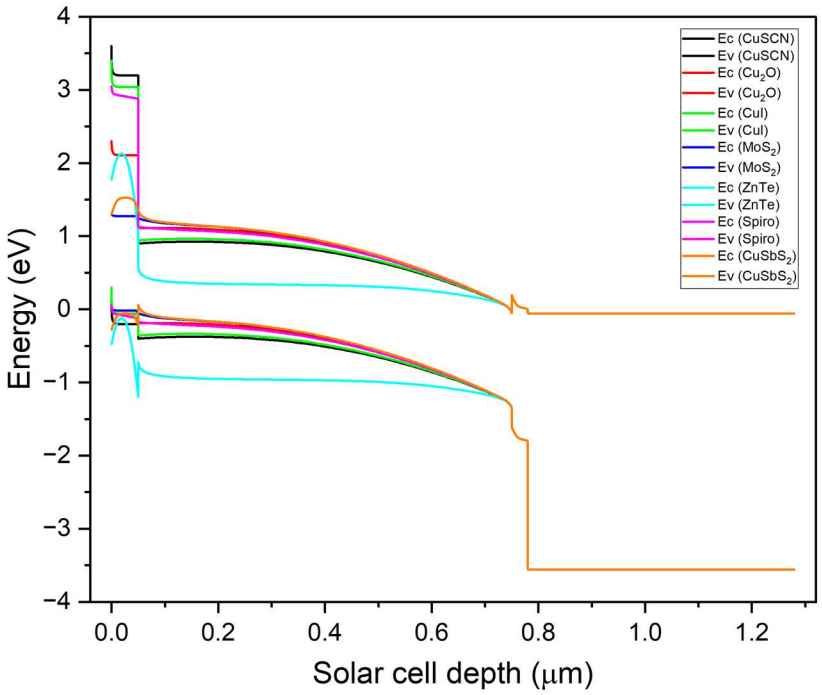

Figure 8. Energy band structure of $CH_3NH_3SnI_3$ solar cells with various HTL materials.

Table 8. Valence band energy offset between $CH_3NH_3SnI_3$ and the HTL layer and the contact barrier at the Ni/HTL interface.

HTL material	HTL/$CH_3NH_3SnI_3$ valence offset (eV)	Ni/ETL contact barrier (Hole) (eV)
CuSCN	0.18	0.2
Cu_2O	0.134	0.13
CuI	0.28	0.36
MoS_2	0.105	0.01
ZnTe	0.791	–0.48
Spiro	0.108	0.05
$CuSbS_2$	0.056	–0.28

3.4. Influence of ETL thickness

The thickness of the ETL layer directly impacts the rate at which electrons pass through from the $CH_3NH_3SnI_3$ layer to the front electrode. An adequately thick ETL can minimize recombination by efficiently removing electrons from the layer made up of perovskite, hence minimizing the probability of their recombination with holes [28]. An ETL layer that is too thin can lead to insufficient electron transport, while an ETL layer that is too thick can impede effective electron flow to the front contact. Additionally, a thick ETL layer can raise series resistance and lower the fill factor, ultimately resulting in less efficiency [29]. The impact of WS_2 thickness on the performance of $CH_3NH_3SnI_3$ solar cells is examined by altering its value within the range of 0.01 to 0.45 μm, while maintaining the thicknesses of the other layers unchanged. Figure 9a displays the J-V curves for solar cells at various thicknesses of WS_2. The graph exhibits nearly identical patterns for all cells with different ETL thicknesses.

Figure 9b demonstrates the impact of ETL thickness on the solar cell parameters. A slight, gradual increase in efficiency is observed with increasing thickness, peaking at 29.778% when the thickness reaches 0.25 µm, followed by a subsequent fall. The decrease in efficiency at greater thickness may be correlated to the rise in the carriers' recombination and the increase in series resistance [30].

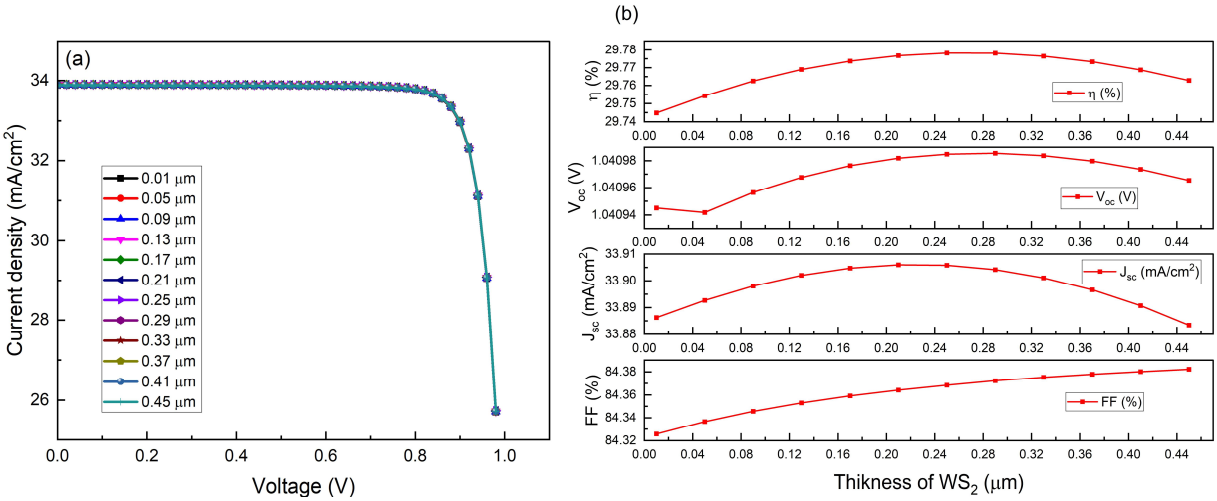

Figure 9. (a) J-V characteristics and (b) V_{oc}, J_{sc}, FF, and η variation with the WS_2 ETL thickness.

The profile of the photogeneration rate of the $CH_3NH_3SnI_3$ cell at various WS_2 ETL thicknesses is plotted against the solar cell depth in Figure 10a. It can be noticed that the photogeneration process takes place at greater depth within the ETL layer as its thickness increases, which indicates that the photons penetrate a deeper distance. The recombination rate with respect to the ETL thickness is plotted in Figure 10b. The recombination process peaks with a higher rate as the ETL thickness increases, which explains the reduction of cell efficiency beyond 0.25 µm, as discussed in Figure 9b.

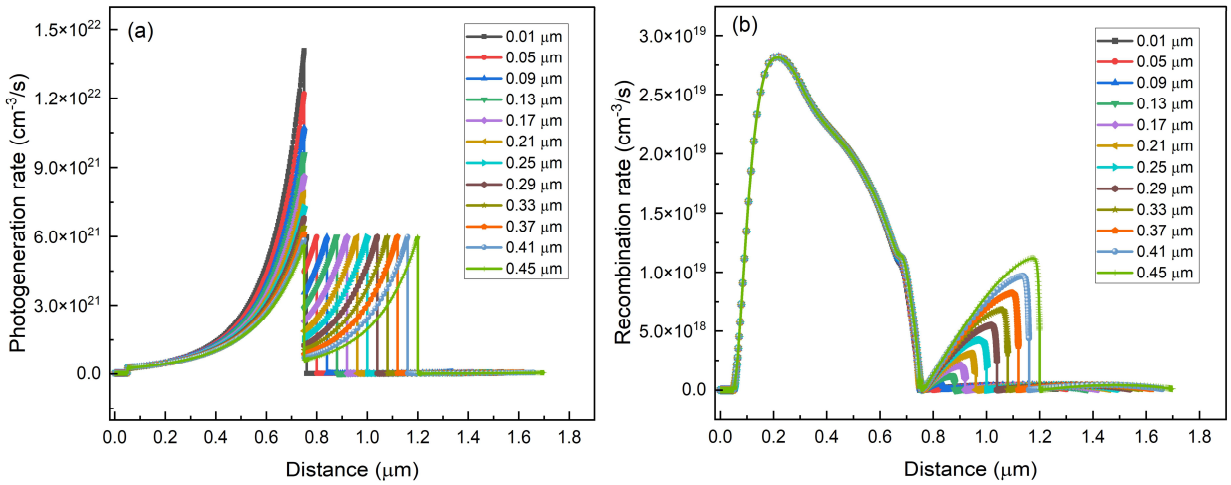

Figure 10. (a) Photogeneration and (b) recombination rates of $CH_3NH_3SnI_3$ solar cell at various WS_2 HTL thicknesses.

3.5. Influence of HTL thickness

An optimal thickness of the HTL promotes efficient delivery of holes throughout the Perovskite material to the terminals. This reduces recombination losses and boosts the functionality of the cell [31]. The study examines the influence of $CuSbS_2$ HTL thickness on the performance of $CH_3NH_3SnI_3$ solar cells. The HTL thickness varies from 0.01 to 0.23 µm, while maintaining the same thickness for the $CH_3NH_3SnI_3$ and FTO layers and utilizing the optimal WS_2 thicknesses. Figure 11a displays the J-V curves for the solar cells at different thicknesses of $CuSbS_2$. The graph demonstrates that the behavior of all cells remains constant throughout various HTL thicknesses, except at 0.01 µm, where there is a noticeably lower V_{oc}. Figure 11b demonstrates the influence of HTL thickness on the solar cell parameters. It is apparent that the cell's efficiency experiences a sharp rise as thickness varies from 0.01 to 0.03 µm, and then continues to slowly increase as thickness increases. The optimal thickness is determined to be 0.21 µm, beyond which increasing the thickness of the HTL does not result in any additional gain in solar cell performance, since the efficiency remains nearly constant [32].

Figure 12a illustrates the profile of the photogeneration rate of the $CH_3NH_3SnI_3$ cell at various $CuSbS_2$ HTL thicknesses. Obviously, the photogeneration process takes place deeper in the solar cell layers as the HTL thickness increases, which indicates that the photons penetrate a deeper distance. The recombination rate with respect to the HTL thickness is plotted in Figure 12b. It can be noticed that the recombination rate does not change with ETL thickness, which indicates that variation in the thickness of the HTL layer in the current solar cell does not impact the cell's efficiency, as discussed in Figure 11.

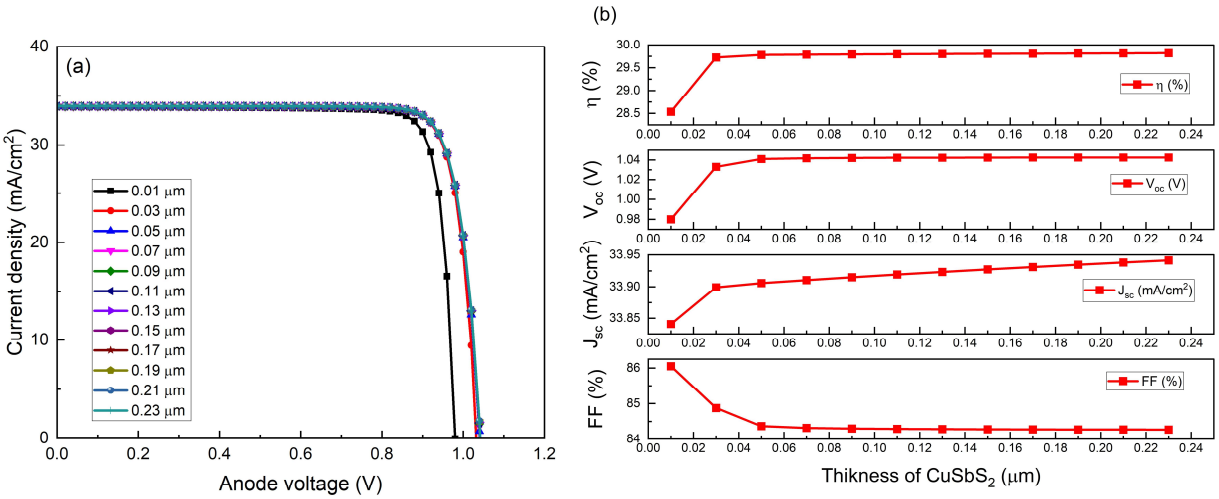

Figure 11. (a) J-V characteristics of $CH_3NH_3SnI_3$ solar cells at different $CuSbS_2$ HTL thicknesses. (b) V_{oc}, J_{sc}, FF, and η variation with $CuSbS_2$ HTL thickness.

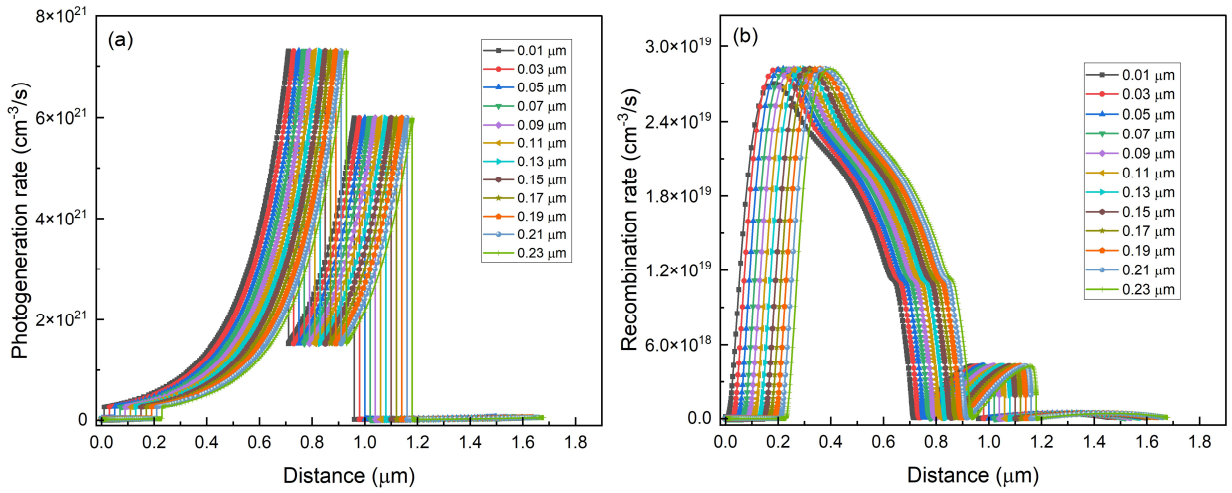

Figure 12. (a) Photogeneration and (b) recombination rate of the $CH_3NH_3SnI_3$ solar cell.

3.6. Influence of ETL doping

The effect of the donor doping in the WS_2 ETL layer on the characteristics of the $CH_3NH_3SnI_3$ solar cell was examined by altering the amount of doping from 1×10^{14} to 1×10^{21} cm^{-3}. Figure 13a displays the J-V behavior of the $CH_3NH_3SnI_3$ solar cell at various amounts of doping in the ETL. It is evident that all the cells exhibit identical curves. Figure 13b displays the plotted results of the doping level of the ETL versus the J_{sc}, V_{oc}, FF, and η. It is visible that the conversion efficiency of the solar cell increases a little, reaching a value of 29.82% as the doping level is 1×10^{18} cm^{-3}. After this point, efficiency remains constant, which indicates that additional increases in doping dosage have no effect on the behavior of the solar cell. Therefore, a doping concentration of 1×10^{18} cm^{-3} is considered to be the best possible value for the WS_2 layer in the current solar cell.

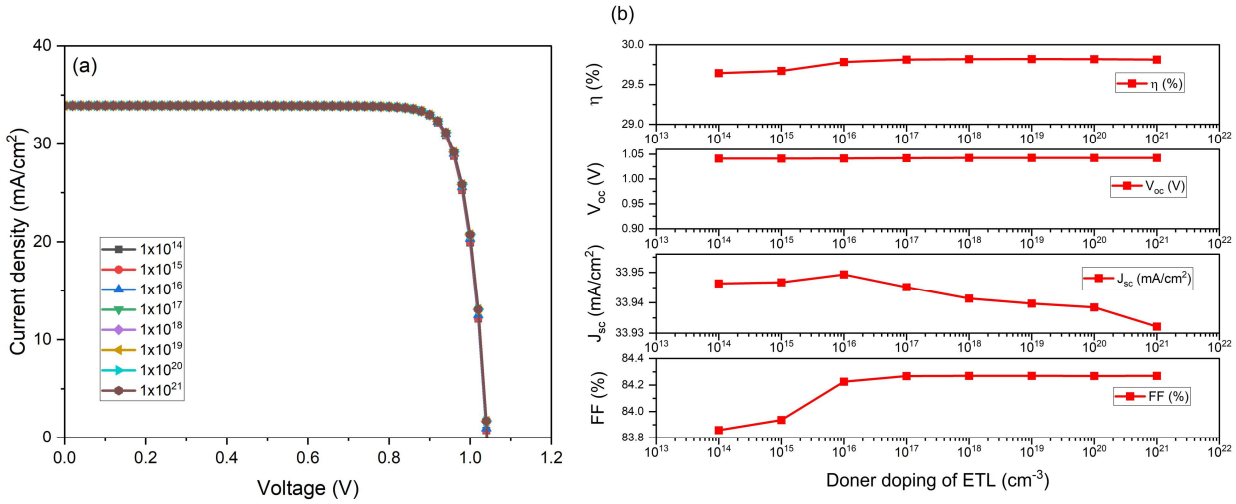

Figure 13. (a) J-V characteristics and (b) V_{oc}, J_{sc}, FF, and η of $CH_3NH_3SnI_3$ solar cell at various WS_2 ETL doping concentrations.

The influence of WS_2 ETL doping concentration on the photogeneration rate is depicted in Figure 14a. Clearly, the photogeneration profile for all cells at different WS_2 doping levels is identical. However, the effect of doping on the ETL layer is evident in the recombination rate, which decreases within the active region as the ETL doping increases, as shown in Figure 14b. The recombination rate in the perovskite layer decreases up to a doping level of 1×10^{17} cm^{-3} and then becomes nearly constant at higher doping levels. This variation in recombination with ETL doping is in line with the efficiency trend discussed in Figure 13b.

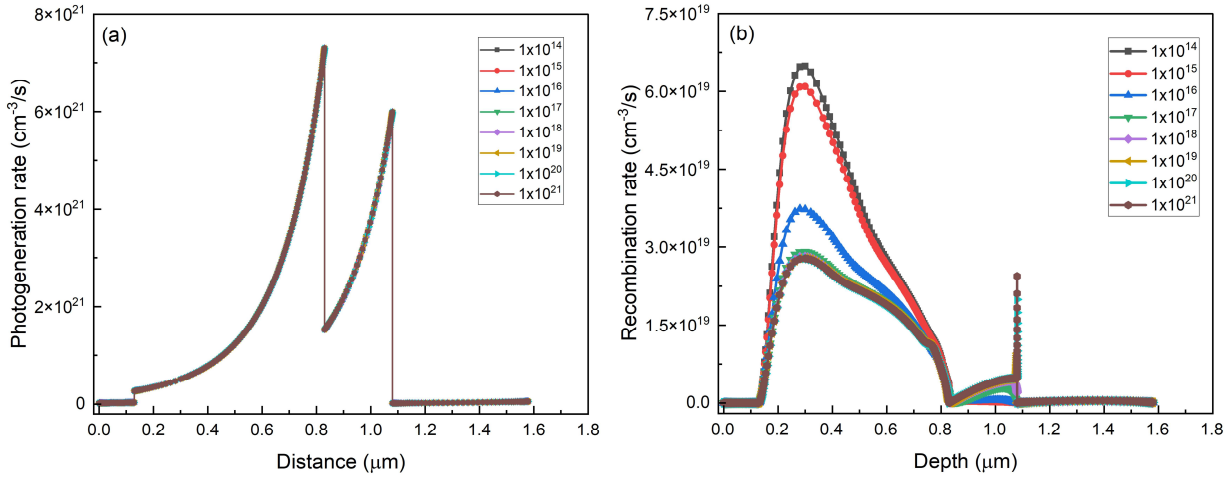

Figure 14. (a) Photogeneration and (b) recombination rate of a $CH_3NH_3SnI_3$ solar cell.

3.7. Impact of HTL doping

The effect of acceptor doping amounts on the operation of $CH_3NH_3SnI_3$ solar cells was investigated by altering the doping values of the $CuSbS_2$ HTL layer from 1×10^{14} to 1×10^{21} cm^{-3}. Figure 15a displays the J-V curves of the $CH_3NH_3SnI_3$ solar cells at various concentrations of HTL doping. It is evident that cells with low injecting concentrations have lower V_{oc} values. Figure 15b illustrates the relationship between the concentration of doping and the variations in J_{sc}, V_{oc}, FF, and η. The findings indicate that the η value of the solar cell increases gradually from 27.82% to 29.82% when doping is 1×10^{18} cm^{-3}. After reaching this value, efficiency stays relatively constant. Consequently, increasing $CuSbS_2$ doping does not have any impact on the efficiency of the solar cell. The most effective doping level of the $CuSbS_2$ HTL layer is considered to be 1×10^{18} cm^{-3}.

The variation of the photogeneration rate with the doping concentration of the $CuSbS_2$ HTL is presented in Figure 16a. The figure shows that the photogeneration profile for all cells at different doping levels of $CuSbS_2$ is identical. To gain more insight into the behavior of the solar cells at different doping concentrations, the recombination rate as a function of the cell's depth is plotted in Figure 16b. The carrier recombination within the active region decreases with an increase in HTL doping up to 1×10^{17} cm^{-3}; it then attains a constant rate at higher doping levels. This variation in the recombination rate with HTL doping agrees with the efficiency trend discussed for Figure 13b.

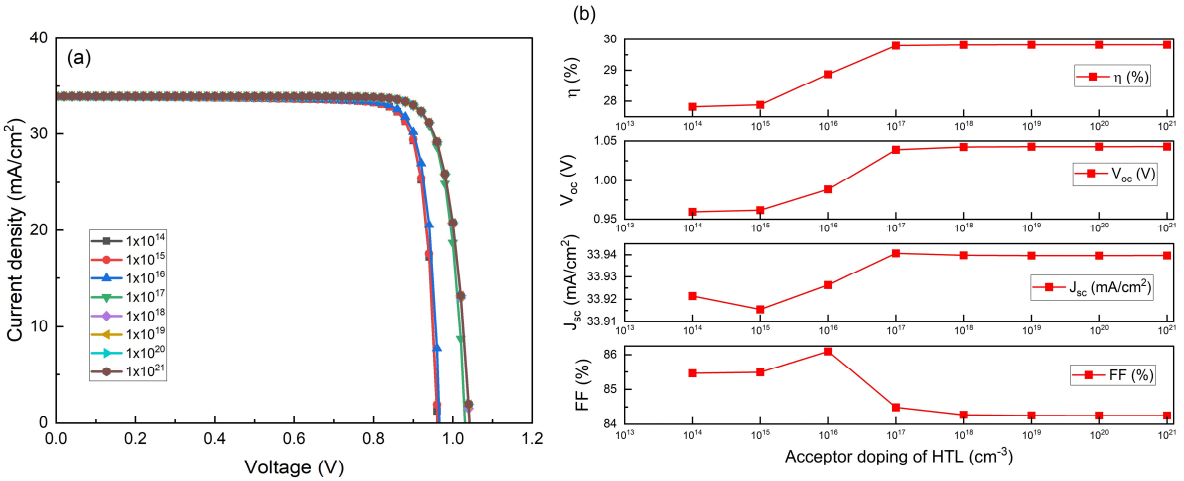

Figure 15. (a) J-V characteristics and (b) V_{oc}, J_{sc}, FF, and η of $CH_3NH_3SnI_3$ solar cell at various $CuSbS_2$ HTL doping concentrations.

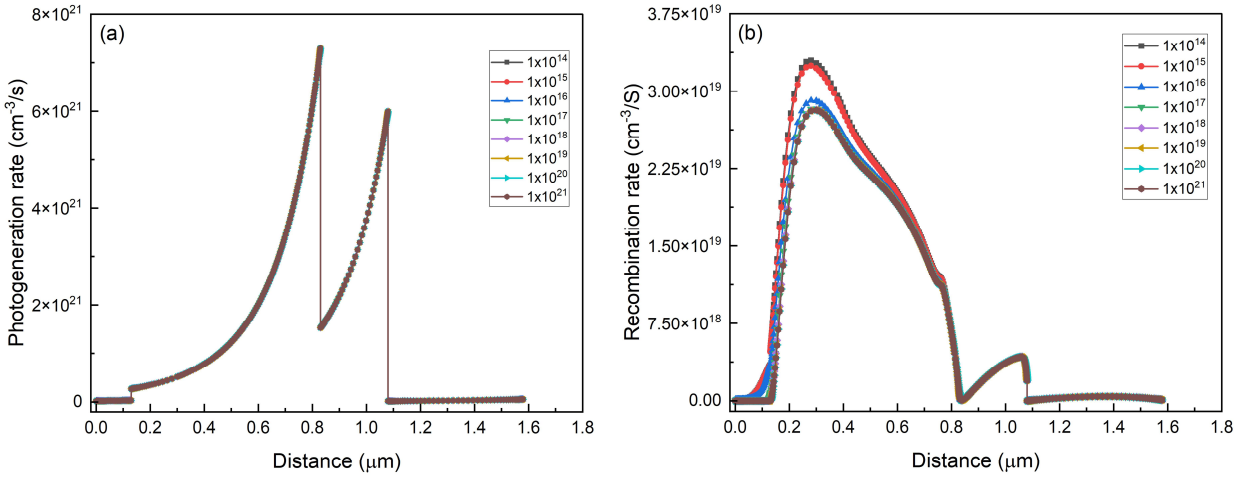

Figure 16. (a) Photogeneration and (b) recombination rate of $CH_3NH_3SnI_3$ solar cell at various $CuSbS_2$ HTL doping concentrations.

3.8. Optimized solar cell

Following the optimization of the ETL and HTL thickness and doping level, a simulation of the optimum $CH_3NH_3SnI_3$ solar cell has been conducted. The resulting J-V characteristics are displayed in Figure 17a. The optimized solar cell exhibits improved electrical parameters compared to the initially suggested solar cell. Specifically, the V_{oc} rises from 1.024 to 1.042 V, the J_{sc} increases from 33.86 to 33.92 mA/cm^2, the FF rises from 76.17% to 84.29%, and η improves from 26.42% to 29.8%. These findings demonstrate that selecting appropriate ETL and HTL materials, along with optimizing their thickness and doping concentrations, directly affects the functionality of $CH_3NH_3SnI_3$ solar cells. The relationship between quantum efficiency and wavelength fluctuation reveals a behavior that is identical to that of the basic solar cell, as illustrated in Figure 17b.

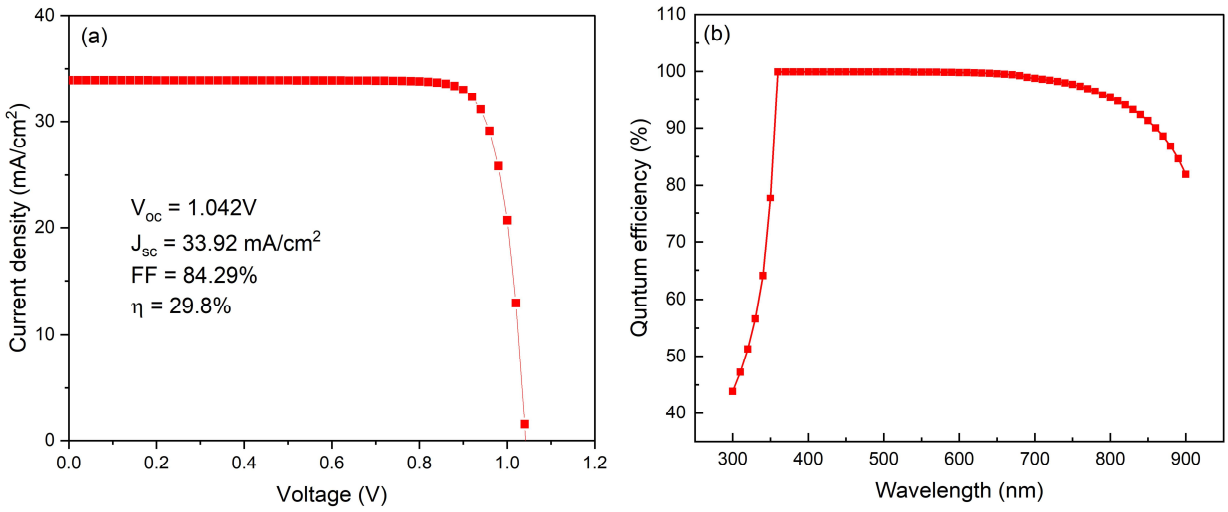

Figure 17. (a) J-V characteristics and (b) efficiency versus wavelength of the optimized $CH_3NH_3SnI_3$ solar cell.

4. Conclusions

Simulation-based research was conducted to study the impact of the material, thickness, and doping level of the ETL and HTL on the operating characteristics of the $CH_3NH_3SnI_3$ solar cell. This task was carried out via the SCAPS-1D software, where the solar cell was illuminated with AM1.5G spectra at an intensity of 1000 W/m^2. The results indicate that the best performance for $CH_3NH_3SnI_3$ solar cells is achieved when WS_2 is used as the ETL and $CuSbS_2$ as the HTL. Optimizing the materials used in the ETL and HTL layers reveals that increasing the doping level and thickness of these layers leads to a slight improvement in the performance of the $CH_3NH_3SnI_3$ solar cell. The electrical parameters of the $CH_3NH_3SnI_3$ solar cell show improvements compared with the initial solar cell. The V_{oc} improves from 1.024 to 1.042 V, J_{sc} increases from 33.86 to 33.92 mA/cm^2, the FF improves from 76.17% to 84.29%, and η improves from 26.42% to 29.8%. These findings indicate that optimizing the ETL and HTL in terms of material selection, thickness, and doping concentration plays a critical role in determining the performance characteristics of $CH_3NH_3SnI_3$-based solar cells.

Use of AI tools declaration

The authors declare they have not used Artificial Intelligence (AI) tools in the creation of this article.

Author contributions

Ala'eddin A. Saif: supervision, project administration, investigation, methodology, formal analysis, writing–review & editing; Ghalyiah Alahmadi: methodology, data collections, investigation.

Conflict of interest

The authors declare no conflict of interest.

References

1. Rono N, Merad AE, Kibet JK, et al. (2021) A theoretical investigation of the effect of the hole and electron transport materials on the performance of a lead-free perovskite solar cell based on $CH_3NH_3SnI_3$. *J Comput Electron* 20: 993–1005. https://doi.org/10.1007/s10825-021-01673-z
2. Casas GA, Cappelletti MA, Cedola AP, et al. (2017) Analysis of the power conversion efficiency of perovskite solar cells with different materials as hole-transport layer by numerical simulations. *Superlattice Microst* 107: 136–143. https://doi.org/10.1016/j.spmi.2017.04.007
3. Green MA, Dunlop ED, Hohl-Ebinger J, et al. (2023) Solar cell efficiency tables (version 62). *Prog Photovolt Res Appl* 31: 3–16. https://doi.org/10.1002/pip.3646
4. Xu K (2021) Development of tin-based perovskite materials for solar cell applications: A minireview. *Instrum Sci Technol* 49: 91–105. https://doi.org/10.1080/10739149.2020.1785891
5. Patel PK (2021) Device simulation of highly efficient eco-friendly $CH_3NH_3SnI_3$ perovskite solar cell. *Sci Rep* 11: 3082. https://doi.org/10.1038/s41598-021-82817-w
6. Mottakin M, Sobayel K, Sarkar D, et al. (2021) Design and modelling of eco-friendly $CH_3NH_3SnI_3$-based perovskite solar cells with suitable transport layers. *Energies* 14: 7200. https://doi.org/10.3390/en14217200
7. Chen L, Fu S, Li Y, et al. (2024) On the durability of tin-containing perovskite solar cells. *Adv Sci* 11: 202304811. https://doi.org/10.1002/advs.202304811
8. Zhou T, Huang X, Yao R, et al. (2025) Integrative enhancement of energy-level alignment and defect passivation for high-performance lead-free perovskite solar cells. *Adv Theory Simul* 8: 2401064. https://doi.org/10.1002/adts.202401064
9. Howlader AH, Dipta SS, Tarique WB, et al. (2024) Self-formation of $SnCl_2$ passivation layer on SnO_2 electron-transport layer in chloride–iodide-based perovskite solar cell. *Adv Energy Sustain Res* 5: 2400030. https://doi.org/10.1002/aesr.202400030
10. Dipta SS, Rahaman MH, Tarique WB, et al. (2024) Highly efficient double-side-passivated perovskite solar cells for reduced degradation and low photovoltage loss. *Sol Energy Mater Sol Cells* 266: 112655. https://doi.org/10.1016/j.solmat.2023.112655
11. Ayad M, Fathi M, Mellit A (2021) Study and performance analysis of perovskite solar cell structure based on organic and inorganic thin films. *Optik* 233: 166619. https://doi.org/10.1016/j.ijleo.2021.166619
12. Huang ZP, Chen YX, Huang ZH, et al. (2023) Simulation of highly efficient GeSe-based solar cells with SCAPS-1D. *Heliyon* 9: e18776. https://doi.org/10.1016/j.heliyon.2023.e18776
13. Lenka TR, Soibam AC, Dey K, et al. (2020) Numerical analysis of high efficiency lead-free perovskite solar cell with NiO as hole transport material and PCBM as electron transport material. *CSIT* 8: 111–116. https://doi.org/10.1007/s40012-020-00291-7
14. Karimi E, Ghorashi SMB (2017) Investigation of the influence of different hole transporting materials on the performance of perovskite solar cells. *Optik* 130: 650–658. https://doi.org/10.1016/J.IJLEO.2016.10.122
15. Karthick S, Velumani S, Boucle J (2020) Experimental and SCAPS simulated for mamidinium perovskite solar cells: A comparison of device performance. *Sol Energy* 205: 349–357. https://doi.org/10.1016/j.solener.2020.05.041

16. Dipta SS, Howlader AH, Tarique WB, et al. (2025) Evaluating different alkylammonium bromide passivation films to stabilize and enhance PV performance of perovskite solar cells. *Sol Energy* 286: 113195. https://doi.org/10.1016/j.solener.2024.113195
17. Tarique WB, Rahaman MH, Dipta SS, et al. (2024) Solution-processed bilayered ZnO electron transport layer for efficient inverted non-fullerene organic solar cells. *Nanomanufacturing* 4: 81–98. https://doi.org/10.3390/nanomanufacturing4020006
18. Valeti NJ, Prakash K, Singha MK (2023) Numerical simulation and optimization of lead free $CH_3NH_3SnI_3$ perovskite solar cell with $CuSbS_2$ as HTL using SCAPS 1D. *Results Opt* 12: 100440. https://doi.org/10.1016/j.rio.2023.100440
19. Gagandeep, Singh M, Kumar R, et al. (2021) Investigation of $CH_3NH_3PbI_3$ and $CH_3NH_3SnI_3$ based perovskite solar cells with $CuInSe_2$ nanocrystals. *Optik* 246: 167839. https://doi.org/10.1016/j.ijleo.2021.167839
20. Zainal Abidin NA, Arith F, Noorasid NS, et al. (2023) Dopant engineering for ZnO electron transport layer towards efficient perovskite solar cells. *RSC Adv* 13: 33797–33819. https://doi.org/10.1039/d3ra04823c
21. Rai N, Rai S, Singh PK, et al. (2020) Analysis of various ETL materials for an efficient perovskite solar cell by numerical simulation. *J Mater Sci Mater Electron* 31: 16269–16280. https://doi.org/10.1007/s10854-020-04175-z
22. Mercy PAM, Wilson KSJ (2023) Development of environmental friendly high performance Cs_2TiBr_6 based perovskite solar cell using numerical simulation. *Appl Surf Sci Adv* 15: 100394. https://doi.org/10.1016/j.apsadv.2023.100394
23. Bag A, Radhakrishnan R, Nekovei R, et al. (2020) Effect of absorber layer, hole transport layer thicknesses, and its doping density on the performance of perovskite solar cells by device simulation. *Sol Energ* 196: 177–182. https://doi.org/10.1016/j.solener.2019.12.014
24. Krishna BG, Ghosh DS, Tiwari S (2023) Hole and electron transport materials: A review on recent progress in organic charge transport materials for efficient, stable, and scalable perovskite solar cells. *Chem Inorg Mater* 1: 100026, https://doi.org/10.1016/j.cinorg.2023.100026
25. Li S, Cao YL, Li WH, et al. (2021) A brief review of hole transporting materials commonly used in perovskite solar cells. *Rare Met* 40: 2712–2729. https://doi.org/10.1007/s12598-020-01691-z
26. Zhang B, Zhou Y, Xue Q, et al. (2019) The energy-alignment engineering in polytriphenylamines-based hole transport polymers realizes low energy loss and high efficiency for all-inorganic perovskite solar cells. *Solar RRL* 3: 1900265. https://doi.org/10.1002/solr.201900265
27. Devi C, Mehra R (2019) Device simulation of lead-free $MASnI_3$ solar cell with $CuSbS_2$ (copper antimony sulfide). *J Mater Sci* 54: 5615–5624. https://doi.org/10.1007/s10853-018-03265-y
28. Yu X, Zou X, Cheng J, et al. (2020) Numerical simulation analysis of effect of energy band alignment and functional layer thickness on the performance for perovskite solar cells with $Cd_{1-x}Zn_xS$ electron transport layer. *Mater Res Express* 7: 105906. https://doi.org/10.1088/2053-1591/abbf12
29. Sławek A, Starowicz Z, Lipinski M (2021) The influence of the thickness of compact TiO_2 electron transport layer on the performance of planar $CH_3NH_3PbI_3$ perovskite solar cells. *Materials* 14: 3295. https://doi.org/10.3390/ma14123295
30. Jamal S, Khan AD, Khan AD (2020) High performance perovskite solar cell based on efficient materials for electron and hole transport layers. *Optik* 218: 164787. https://doi.org/10.1016/j.ijleo.2020.164787

31. Moiz SA, Alshaikh MS, Alahmadi ANM (2023) Simulation design of novel non-fluorine polymers as electron transport layer for lead-free perovskite solar cells. *Polymers* 15: 4387. https://doi.org/10.3390/polym15224387
32. Sabbah H, Arayro J, Mezher R (2022) Simulation and investigation of 26% efficient and robust inverted planar perovskite solar cells based on $GA_{0.2}FA_{0.78}SnI_3$-1%$EDAI_2$ films. *Nanomater* 12: 3885. https://doi.org/10.3390/nano12213885

AIMS Press